Frozen patterns of impacted droplets: From conical tips to toroidal shapes

Man Hu,[1] Feng Wang,[1] Qian Tao,[1] Li Chen ⓘ,[1] Shmuel M. Rubinstein,[2] and Daosheng Deng ⓘ[1,*]

[1]*Department of Aeronautics and Astronautics, Fudan University, Shanghai 200433, China*
[2]*John A. Paulson School of Engineering and Applied Sciences, Harvard University, Cambridge,*
Massachusetts 02138, USA

We report frozen ice patterns for the water droplets impacting on a cold substrate through high-speed images. These patterns can be manipulated by several physical parameters (the droplet size, falling height, and substrate temperature), and the scaling analysis has a remarkable agreement with the phase diagram. The observed double-concentric toroidal shape is attributed to the correlation between the impacting dynamics and freezing process, as confirmed by the spatiotemporal evolution of the droplet temperature, the identified timescale associated with the morphology and solidification ($t_{inn} \simeq \tau_{sol}$), and the ice front-advection model. These results for frozen patterns provide insight into the complex interplay of the rapid impacting hydrodynamics, the transient heat transfer, and the intricate solidification process.

Over the past decade, the elegant and beautiful splashing patterns during water droplets impacting on a solid substrate at room temperature have been extensively investigated [1–4]. Recently, the study of droplets impacting on a cold substrate has emerged, and many fascinating and intriguing physical phenomena have been revealed [5–8]. For example, the universal ice-cone formation of freezing droplets is characterized by a tip singularity due to the geometric confinement of the freezing fronts [5]. As the substrate temperature is sufficiently low, the crack pattern is observed in the form of fragmentation or hierarchical fracture [6]. By controlling the thermal properties of the substrate, the self-peeling of impacting droplets occurs [7]. A peculiar freezing morphology at the liquid-solid interface, as explored by the total internal reflection technique, is explained by an ice front-advection model due to the rapid growth of crystals and the sequential advection by internal viscous flow [8]. These scientific advancements have the promising implications for the relevant technologies, such as icing and anti-icing [9,10], or solidification for liquid metals and three-dimensional (3D) printing [11–15].

In this Rapid Communication, we report frozen ice patterns for the droplets falling from various heights on a cold substrate through high-speed images. These patterns can be controlled by several physical parameters (the droplet size, falling height, and the substrate temperature), and their transition can be remarkably described by a simple power law from the scaling analysis. The observed double-concentric toroidal shape is attributed to the strong correlation between the impacting hydrodynamics and solidification process, as confirmed by the spatiotemporal evolution of the droplet temperature, the identified timescale associated with the morphology and solidification ($t_{inn} \simeq \tau_{sol}$), and the ice front-advection model.

The experiments were performed at room temperature, and the substrate temperature ($T_s < 0\,^\circ\text{C}$) was controlled by partially immersing the aluminium plate into liquid nitrogen. The outlet of the
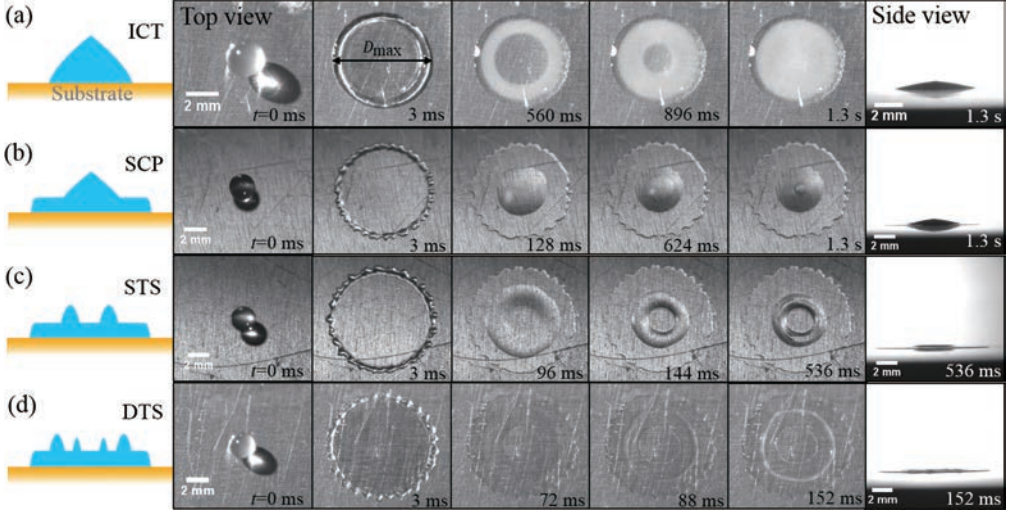
---

*dsdeng@fudan.edu.cn

FIG. 1. Four frozen patterns are visualized by the high-speed images for the spreading dynamics and the subsequent solidification process during the droplet impacted on a cold substrate at $T_s = -15\,°C$. (a) Ice with a conical tip, (b) a spherical cap on the pancake, (c) a single toroidal shape, and (d) a double-concentric toroidal shape for $H_0 = 10, 35, 70,$ and 80 cm, respectively. $t = 0$ ms is defined as droplets landing on or starting to impact on the substrate, as shown by the first-column images.

micrometer syringe (Gillmont GS-1200, Cole-Parmer Inc, 2 ml) is connected with a needle, the inner diameter of which controls the droplet size (volume V_0 or diameter $D_0 = 2R_0$). Then the distilled water droplet was released to impact on the cold substrate [16].

The impacting dynamics is captured by high-speed cameras (Phantom V611) from the top view and the side view (Fig. 1), and four types of frozen patterns are identified for the droplets ($D_0 = 2R_0 \approx 2.4$ mm) released at various heights $H_0 = 10, 35, 70,$ and 80 cm ($T_s = -15\,°C$) (see the Supplemental Material [16] for videos). For the lowest $H_0 = 10$ cm [Fig. 1(a)], the droplet impacts on the cold substrate ($t = 0$ ms) and spreads outward radially until reaching its maximum diameter (D_{max}) at $t = 3$ ms. Since the ice-water front moves radially toward its center during solidification, the droplet is gradually frozen into ice, while a pointy tip (side view) is formed [5]. Eventually, the final frozen pattern is the ice with a conical tip (ICT).

For the increased $H_0 = 35$ cm [Fig. 1(b)], after spreading to D_{max}, its spreading edge is pinned to subject the regime of the stationary contact line rather than recoiling immediately [17]. During the stationary contact line period (τ_{SCL}), the underneath liquid is directly contacted with the cold substrate, resulting in the growth of the bottom-pancake ice. After the stationary contact line stage, the remaining top-layer liquid with larger aspect ratio is unstable due to surface tension and retracts to form a spherical cap, while the pointy tip still appears at the final freezing stage (side view). Then, the frozen pattern [17,18] is a spherical cap on the pancake (SCP).

However, at much higher H_0, more intriguing final frozen patterns are observed that the distinctive toroidal shapes together with the inner holes (or the inner valley regions), as clearly visible in Fig. 1(c) and 1(d). For $H_0 = 70$ cm [Fig. 1(c)], the frozen pattern is exemplified by a single toroidal shape (STS) (the ring pattern [18] or the central-concave profile [19]), reminiscent of a doughnut shape during the impacted droplets at room temperature [20] or during laser-induced forward transfer [21]. For $H_0 = 80$ cm [Fig. 1(d)], the frozen pattern is represented by an intriguing double-concentric toroidal shape (DTS).

In order to understand the observed toroidal shapes, the dynamics of the outer rim boundary of the top-layer liquid film (its diameter D_{out}) is compared [Fig. 2(a)]. Similar to SCP [17], the stage of the stationary contact line still exists for STS and DTS to form the bottom-pancake ice, and
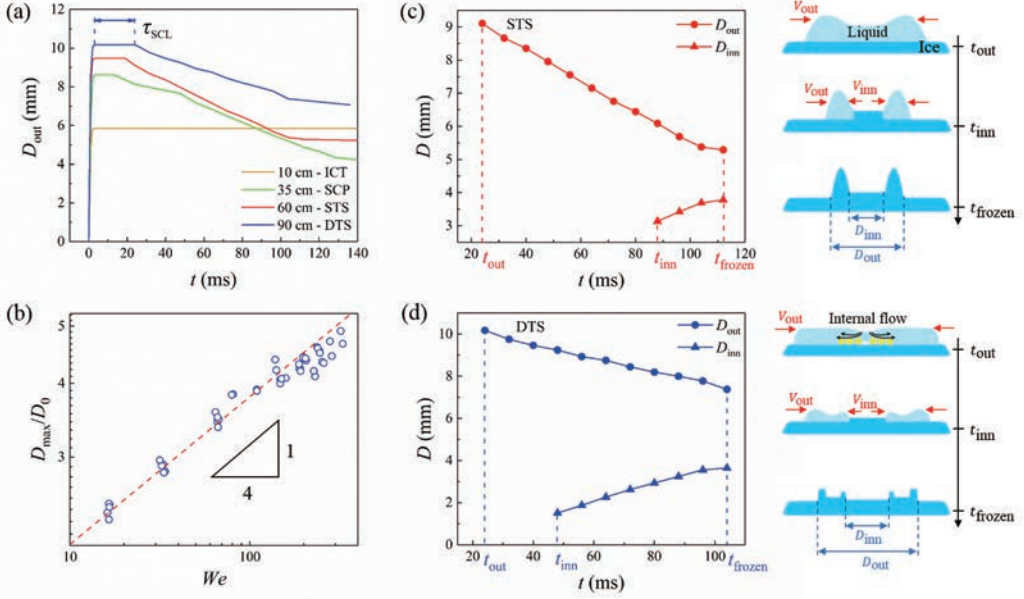
FIG. 2. Formation of toroidal shapes at $T_s = -15\,°\text{C}$. (a) The full dynamics of D_{out}, indicating τ_{SCL} during which the bottom-pancake ice is formed. (b) The scaling law of $D_{\text{max}} \sim \text{We}^{1/4}$. [(c), (d)] Dynamics of D_{out} and D_{inn} for STS and DTS. Sketch mechanism for STS due to the doughnut shape at t_{out}, and for DTS based on the ice front-advection model.

$\tau_{\text{SCL}} = 10^5 \eta(h - 70)/\gamma$ (γ, η for the surface tension [22] and viscosity of water), where the initial liquid thickness h (μm scale here) is expressed as below:

$$h = 4V_0/\pi D_{\text{max}}^2. \tag{1}$$

The calculated $\tau_{\text{SCL}} \approx 23$ ms is comparable with the experimental τ_{SCL} (16 ms for STS and 21 ms for DTS).

Despite the complicated frozen dynamics for these patterns, similar to the drop impacting on solid surface at room temperature [23], the following scaling law for D_{max} holds well [Fig. 2(b)], indicating that the spreading process is dominated by the impact dynamics,

$$D_{\text{max}} \sim D_0 \text{We}^{1/4}, \tag{2}$$

where $\text{We} = \rho R_0 U_0^2/\gamma = 2\rho g H_0 R_0/\gamma$ is Weber number (ρ for the density of water and U_0 for the impacted velocity).

For toroidal shapes, the dynamics of the inner rim boundary of the top-layer liquid (its diameter D_{inn}) is further demonstrated [Fig. 2(c) and 2(d)]. At t_{out} after τ_{SCL}, the spreading edge of the top-layer liquid is unpinned and begins to recoil, resulting in the decreased D_{out} with a constant velocity v_{out} (that is attained by the linear fitting of D_{out} in experiments). Afterward at t_{inn}, the inner hole or the inner rim boundary of the top-layer liquid occurs or is noticeably observed from the high-speed images, and D_{inn} expands radially outward with a constant velocity v_{inn} (that is attained by the linear fitting of D_{inn} in experiments). Then at t_{frozen}, the droplets are completely frozen into the final patterns.

Quantitatively, the experimental velocity of v_{out} and v_{inn} for toroidal shapes is reasonably consistent with the theoretical velocity determined by the viscocapillary balance as confirmed in recent work [18], where the retraction velocity of water film on ice is independent of the thickness of water film. By balancing capillary force and viscous force, the moving velocity of liquid film on
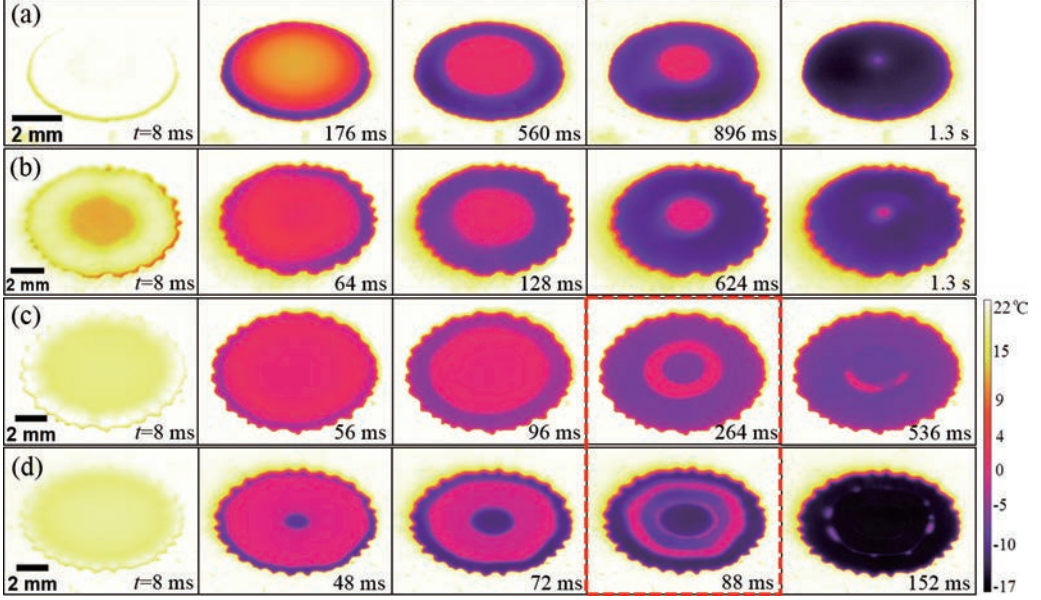
FIG. 3. Spatiotemporal evolution of surface temperature for four patterns demonstrates the correlation between the morphology and temperature distribution. The experimental parameters are the same as those in Fig. 1, and [(a)–(d)] for $H_0 = 10, 35, 70$, and 80 cm, respectively.

ice v $= \gamma \theta_r^3 / 6\eta \ln$ [24,25], where $\theta_r \approx 0.1$ rad is the receding contact angle of water on ice [26], and ln ≈ 1 for a logarithmic factor [24]. Then the theoretical v ≈ 13 mm/s fairly agrees with the experimental values. Additionally, this dynamics and the frozen double-concentric toroidal shapes can be reproduced well (see the Supplemental Material [16]).

By synchronizing a thermal camera with the fast-speed camera (see the Supplemental Material Videos 1–4) [16], the spatial-temporal evolution of the surface temperature for these four patterns (corresponding to Fig. 1) is further demonstrated by thermal images, as shown in Fig. 3. Particularly, the typical snapshot of surface temperature at $t = 264$ ms in Fig. 3(c) and $t = 88$ ms in Fig. 3(d) (the red dashed rectangular) clearly correlates the pattern of STS and DTS, respectively. For ICT, the temperature at the outer ice-water front is $T_{\text{out}} \approx 0°$C. For the other three patterns, although $T_{\text{out}} > 0°$C at the beginning stage of retraction, after a certain period, water is in a supercooling state ($T_{\text{out}} < 0°$C). However, for both STS and DTS, the inner ice-water front is always in a supercooling state ($T_{\text{inn}} < 0°$C) (see the Supplemental Material for surface temperature [16]).

Furthermore, a scaling analysis of $\tilde{D}_0 \sim \tilde{H}_0^\alpha$ is performed to understand a phase diagram of these frozen patterns (Fig. 4), which is obtained by controlling the droplet size (D_0) and falling height (H_0) at $T_s = -20°$C [$\tilde{D}_0 = D_0/k^{-1}, \tilde{H}_0 = H_0/k^{-1}, k^{-1} = (\gamma/\rho g)^{1/2}$ for the capillary length]. Since SCP is characterized by the pinned edge and later unpinning from surface tension, the transition from ICT to SCP is by comparing $D_{\max}$ [Eq. (2)] and the capillary length k^{-1}. Then, $D_{\max} \sim k^{-1}$ leads to $\alpha = -1/5$,

$$\tilde{D}_0 \sim \tilde{H}_0^{-1/5}. \tag{3}$$

Physically, STS [sketch in Fig. 2(c)] is reminiscent of the toroidal shape for a droplet impacting on a superhydrophobic solid surface at room temperature [20]. The faster spreading of the droplet falling at a larger H_0 gives rise to a dry spot or a dry-out hole in the center, which subsequently is subjected to the cooling process and eventually is frozen into the toroidal shape. For this case, the propagation of capillary wave (wavelength $\lambda = \gamma/\rho V^2$) decays quickly and its travel distance
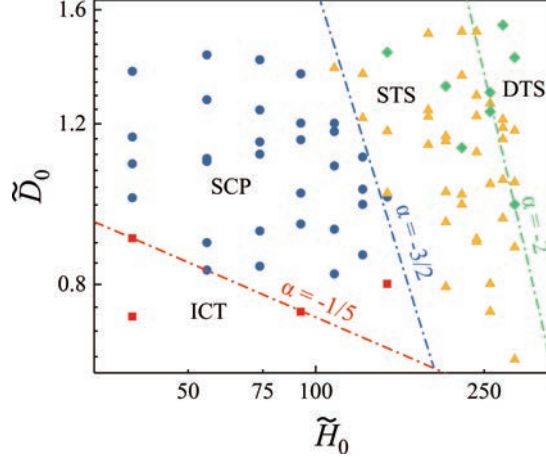
FIG. 4. Phase diagram of frozen patterns dependent on $\tilde{H}_0$ and $\tilde{D}_0$ ($T_s = -20\,^\circ\mathrm{C}$), and their transition described excellently by the scaling law of $\tilde{D}_0 \sim \tilde{H}_0^\alpha$ ($\alpha = -1/5, -3/2, -2$).

($l \sim \rho\lambda^2 V/\eta$) is less than the characterized length scale of the droplet ($l < R$), resulting in $\mathrm{We}\,\mathrm{Ca} > 1$ ($\mathrm{Ca} = \eta U_0/\gamma$) [20]. The physical mechanism of DTS will be addressed more comprehensively later [sketch in Fig. 2(d)]. Hence, the transition criterion from SCP to STS is that $\mathrm{We}\,\mathrm{Ca} \sim 1$, resulting in $\alpha = -3/2$,

$$\tilde{D}_0 \sim \tilde{H}_0^{-3/2}. \tag{4}$$

The transition from STS to DTS is necessary to have a sufficiently faster timescale of solidification ($\tau_{\mathrm{sol}} = h^2/D_s$) [27] to better promote the ice formation for the observed inner holes or dry-out regions. The other relevant parameter is the timescale of the impacting process (τ_{imp}), which is assumed to be the same as the timescale of contacting process for a bouncing drop independent on Weber number $\tau_{\mathrm{imp}} = \tau_{\mathrm{cap}} \sim (\rho D_0^3/\gamma)^{1/2}$ [28]. Then, $\tau_{\mathrm{cap}} \sim \tau_{\mathrm{sol}}$ gives rise to $\alpha = -2$,

$$\tilde{D}_0 \sim \tilde{H}_0^{-2}. \tag{5}$$

Remarkably, this scaling law of $\tilde{D}_0 \sim \tilde{H}_0^\alpha$ ($\alpha = -1/5, -3/2, -2$) in Eqs. (3)–(5) for the pattern transition has an excellent agreement with experiments, as shown by transition lines in Fig. 4.

Besides the droplet sizes and falling heights, these patterns can be manipulated by the substrate temperature. The phase diagram at $T_s = -10\,^\circ\mathrm{C}$ and $-30\,^\circ\mathrm{C}$ (see the Supplemental Material [16]) not only demonstrates that patterns indeed are influenced dramatically by T_s, but also shows that DTS has more tendency to appear at a lower T_s, offering the possibility to achieve the desirable patterns through controlling T_s. Interestingly, despite the complicated effect of T_s, the simple scaling law for the pattern transition still holds for all these three phase diagrams.

Now we proceed to reveal the possible coupling dynamics of the droplet impacting and solidification responsible for the observed DTS. First, the simultaneous snapshots of high-speed imaging and thermal imaging [Fig. 5(a)] are both characterized by a common feature of two concentric rings, clearly demonstrating the correlation between the morphology and frozen process. The spatiotemporal evolution of temperature [Fig. 5(b)] further reveals this feature of two concentric rings at $t = 88$ ms (the red line) and the occurrence of the inner hole at t_{inn} (the dark line) as well.

Second, the experimental t_{inn} associated with the inner ice appearing in the DTS is comparable with the calculated τ_{sol} [27] for the central region of the liquid film to be transformed into ice,
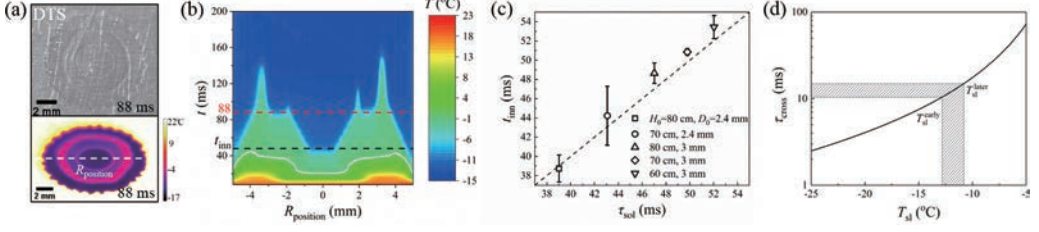
$$t_{\mathrm{inn}} \simeq \tau_{\mathrm{sol}}. \tag{6}$$

FIG. 5. Mechanism of DTS due to the coupling of the droplet impacting hydrodynamics and solidification ($T_s = -15\,°C$). (a) A typical synchronized high-speed image (top) and thermal image (bottom) at $t = 88$ ms, revealing the correlation between the morphology and temperature distribution ($H_0 = 80$ cm). (b) Spatiotemporal evolution of the observed temperature along a horizontal line $R_{position}$ in panel (a), the white line for the zero isotherm. (c) The identified $t_{inn} \simeq \tau_{sol}$, and error bars for three experiments. (d) The calculated τ_{cross} from Eq. (8) around 10 ms corresponding to T_{sl} from the heat transfer model.

This identified timescale relationship is verified by more experiments for DTS produced at various parameters, such as H_0 and D_0 [Fig. 5(c)], evidently showing the strong correlation between impacting dynamics and freezing process.

Third, from a perspective of freezing kinetics, an ice front-advection model [8] is applied here to further understand DTS by considering the classical nucleation theory and the large-scale hydrodynamics on the droplet scale [sketch in Fig. 2(d)]. During a crossover timescale (τ_{cross}), the ice size increases to be comparable with the thickness of the viscous boundary layer, and subsequently this advection of ice front at the substrate-liquid (water) interface should be related with the final frozen patterns.

From the classical nucleation theory, the growth rate of ice (v_g) is as below:

$$v_g(T_{sl}) = \frac{dr}{dt} = \frac{D}{\lambda}\left[1 - \exp\left\{-\frac{M\Delta G_{f,v}}{\rho N_A k_B T_{sl}}\right\}\right], \tag{7}$$

where $T_m = 0\,°C$ is the melting temperature of water, T_{sl} is the temperature at the substrate-liquid interface, and $\Delta G_{f,v} \sim (T_m - T_{sl})$ is the volumetric free-energy difference between solid and liquid [29]. Then the ice size is $r_c = v_g t$ for a given T_{sl}, while the thickness of the viscous boundary layer grows as $\delta_v \sim \sqrt{\eta t/\rho}$ inside an impacting droplet [30]. The relationship between τ_{cross} and T_{sl} is obtained from $r_c \sim \delta_v$ [8],

$$\tau_{cross}(T_{sl}) \sim \frac{\eta}{\rho v_g^2}. \tag{8}$$

Based on simplified heating transfer models ($T_s = -15\,°C$) [8] (see the Supplemental Material [16] for 1D model to obtain T_s), $T_{sl}^{early} \approx -12.8\,°C$ at the early stage by neglecting the latent heat from the heat diffusion model, while $T_{sl}^{later} \approx -10.8\,°C$ at the later stage by including the released latent heat from a 1D two-phase Stefan model using Schwartz solution. According to the temperature zone between T_{sl}^{early} and T_{sl}^{later} [Fig. 5(d)], the estimated $\tau_{cross} \approx 10$ ms is the same order of magnitude as the experimental t_{inn}.

In conclusion, we investigate frozen ice patterns for the water droplets impacting on a cold substrate through high-speed images. These patterns can be manipulated by several physical parameters (the droplet size, falling height, and substrate temperature), and the scaling analysis has a remarkable agreement with the phase diagram. The observed double-concentric toroidal shape is attributed to the correlation between the impacting dynamics and freezing process, as confirmed by the spatiotemporal evolution of the droplet temperature, the identified timescale associated with the morphology and solidification ($t_{inn} \simeq \tau_{sol}$), and the ice front-advection model. These results for frozen patterns provide insight into the complex interplay of the rapid impacting hydrodynamics, the transient heat transfer, and the intricate solidification process.

M.H. and F.W. contributed equally to this work.

[1] A. L. Yarin, Drop impact dynamics: Splashing, spreading, receding, bouncing, Annu. Rev. Fluid Mech. **38**, 159 (2006).

[2] C. Josserand and S. T. Thoroddsen, Drop impact on a solid surface, Annu. Rev. Fluid Mech. **48**, 365 (2016).

[3] L. Xu, W. W. Zhang, and S. R. Nagel, Drop Splashing on a Dry Smooth Surface, Phys. Rev. Lett. **94**, 184505 (2005).

[4] J. M. Kolinski, S. M. Rubinstein, S. Mandre, M. P. Brenner, D. A. Weitz, and L. Mahadevan, Skating on a Film of Air: Drops Impacting on a Surface, Phys. Rev. Lett. **108**, 074503 (2012).

[5] A. G. Marin, O. R. Enriquez, P. Brunet, P. Colinet, and J. H. Snoeijer, Universality of Tip Singularity Formation in Freezing Water Drops, Phys. Rev. Lett. **113**, 054301 (2014).

[6] E. Ghabache, C. Josserand, and T. Séon, Frozen Impacted Drop: From Fragmentation to Hierarchical Crack Patterns, Phys. Rev. Lett. **117**, 074501 (2016).

[7] J. de Ruiter, D. Soto, and K. K. Varanasi, Self-peeling of impacting droplets, Nat. Phys. **14**, 35 (2018).

[8] P. Kant, R. B. Koldeweij, K. Harth, Michiel AJ van Limbeek, and D. Lohse, Fast-freezing kinetics inside a droplet impacting on a cold surface, Proc. Nat. Acad. Sci. USA **117**, 2788 (2020).

[9] T. Cebeci and F. Kafyeke, Aircraft icing, Annu. Rev. Fluid Mech. **35**, 11 (2003).

[10] T. Vasileiou, T. M. Schutzius, and D. Poulikakos, Imparting icephobicity with substrate flexibility, Langmuir **33**, 6708 (2017).

[11] S. H. Davis, *Theory of Solidification* (Cambridge University Press, Cambridge, UK, 2001).

[12] S. D. Aziz and S. Chandra, Impact, recoil and splashing of molten metal droplets, Int. J. Heat Mass Transf. **43**, 2841 (2000).

[13] S. Haferl and D. Poulikakos, Experimental investigation of the transient impact fluid dynamics and solidification of a molten microdroplet pile-up, Int. J. Heat Mass Transf. **46**, 535 (2003).

[14] M. Vaezi, H. Seitz, and S. F. Yang, A review on 3d micro-additive manufacturing technologies, Inte. J. Adv. Manufacturing Technol. **67**, 1721 (2013).

[15] M. V. Gielen, R. de Ruiter, R. B. Koldeweij, D. Lohse, J. H. Snoeijer, and H. Gelderblom, Solidification of liquid metal drops during impact, J. Fluid. Mech. **883**, A32 (2020).

[16] See Supplemental Material at http://link.aps.org/supplemental/10.1103/PhysRevFluids.5.081601 for experimental methods.

[17] V. Thiévenaz, T. Séon, and C. Josserand, Solidification dynamics of an impacted drop, J. Fluid Mech. **874**, 756 (2019).

[18] V. Thiévenaz, C. Josserand, and T. Séon, Retraction and freezing of a water film on ice, Phys. Rev. Fluids **5**, 041601(R) (2020).

[19] Y. H. Shang, X. F. Liu, B. F. Bai, and X. Zhong, Central-pointy to central-concave icing transition of an impact droplet by increasing surface subcooling, Int. Commun. Heat Mass Transfer **108**, 104326 (2019).

[20] Y. Renardy, S. Popinet, L. Duchemin, M. Renardy, S. Zaleski, C. Josserand, M. A. Drumright-Clarke, D. Richard, C. Clanet, and D. Quéré, Pyramidal and toroidal water drops after impact on a solid surface, J. Fluid Mech. **484**, 69 (2003).

[21] C. W. Visser, R. Pohl, C. Sun, G. W. Römer, B. Huis in t Veld, and D. Lohse, Toward 3d printing of pure metals by laser-induced forward transfer, Adv. Mater. **27**, 4087 (2015).

[22] Indeed, the surface tension at water-ice interface or at a liquid-solid phase transition front is extremely complicated [18], and its value is sensitively dependent on temperature. To simplify the analysis here, the surface tension is taken as a constant at room temperature.

[23] C. Clanet, C. Béguin, D. Richard, and D. Quéré, Maximal deformation of an impacting drop, J. Fluid Mech. **517**, 199 (2004).

[24] P. G. De Gennes, F. Brochard-Wyart, and D. Quéré, *Capillarity and Wetting Phenomena: Drops, Bubbles, Pearls, Waves* (Springer Science & Business Media, Berlin, 2013).

[25] J. H. Snoeijer and J. Eggers, Asymptotic analysis of the dewetting rim, Phys. Rev. E **82**, 056314 (2010).

[26] C. A. Knight, The contact angle of water on ice, J. Colloid Inte. Sci. **25**, 280 (1967).

[27] $\tau_{\text{sol}} = h^2/D_s$, where h is the initial liquid film thickness corresponding to $D_{\max}$ in Eq. (2). $D_s = 2\lambda_s \Delta T/(\rho_s L)$, λ_s for the thermal conductivity of ice, $\Delta T = T_m - T_s$ for the temperature difference between the melting temperature of water T_m and substrate temperature T_s ($= -15\,^\circ\text{C}$), ρ_s is the density of ice, and L is the ice-water latent heat per unit mass [6].

[28] D. Richard, C. Clanet, and D. Quere, Contact time of a bouncing drop, Nature (London) **417**, 811 (2002).

[29] M is the molar mass of water, N_A is the Avegadro constant, k_B is the Boltzmann coefficient, λ is the mean free path of a liquid molecule, D is the diffusion coefficient, $\Delta G_{f,v} = L_v(T_m - T_{sl})$ is the volumetric free-energy difference between solid and liquid, and L_v is the latent heat released per unit volume.

[30] I. V. Roisman, Inertia dominated drop collisions. II. An analytical solution of the Navier-Stokes equations for a spreading viscous film, Phys. Fluids **21**, 052104 (2009).